



OPEN

Transcriptome profiling and characterization of peritoneal metastasis ovarian cancer xenografts in humanized mice

Sung Wan Kang^{1,2}, Ji-young Lee^{1,2}, Ok-Ju Kang^{1,2}, Yong-Man Kim^{1,2}, Eun Kyung Choi^{2,3} & Shin-Wha Lee^{1,2}

Although immunotherapy has not yet been as successful in ovarian cancer (OC), it remains a potential therapeutic strategy. Preclinical models of OC are necessary to evaluate the efficacy of immuno-oncology (IO) drugs targeting human immune components but have been underutilized. Developing mouse models with a humanized (Hu) immune system can help understand the human immune response to IO drugs which have demonstrated limited effectiveness in OC patients. We established OC xenograft Hu-mouse models by intraperitoneally injecting luciferase-expressing SKOV-3 Luc and OVCAR-3 Luc OC cells into CD34⁺ Hu-mice. Tumor growth was monitored through bioluminescence imaging (BLI). In the SKOV-3 Luc Hu-mouse model, we assessed the efficacy of PD-1 blockade with pembrolizumab. We observed the presence of human lymphocyte and myeloid cell subsets within the tumors, lymph nodes, blood, and spleens in these models. Notably, these tumors exhibited a high prevalence of tumor-infiltrating macrophages. Furthermore, we identified HDAC class I target genes, and genes associated with epithelial-mesenchymal transition (EMT) and fibroblasts in the tumors of Hu-mice treated with pembrolizumab. Our xenograft Hu-mouse model of OC provides a valuable tool for investigating the efficacy of IO drugs. The insights gained from this model offer useful information to explore potential mechanisms associated with unresponsive anti-PD-1 treatment in OC.

Ovarian cancer (OC) is the deadliest gynecologic malignancy. Approximately 70% of OC cases are diagnosed at an advanced stage due to the lack of distinct symptoms before metastasis to distant regions^{1,2}. The standard treatment for OC typically comprises debulking surgery and chemotherapy involving platinum and taxane, with the recent addition of poly (ADP-ribose) polymerase (PARP) inhibitors. Despite an initial positive response to these standard treatments in patients with advanced-stage OC, recurrence is frequent, resulting in a 5-year survival rate of less than 50%^{3,4}.

Immunotherapy has emerged as a promising therapeutic intervention for cancer treatment. Approaches such as immune checkpoint inhibitors (ICIs) therapy, infusion of tumor-infiltrating lymphocytes (TILs), mRNA vaccination, and adoptive T-cell therapies using chimeric antigen receptors (CARs) or engineered T-cell receptors (TCRs) are being explored in various cancer patients^{5,6}. Notably, the PD-1/PD-L1 blockade has significantly improved overall survival in certain cancers such as non-small cell lung cancer and melanoma^{7,8}. OC is generally classified as an immunogenic tumor, and an increase in CD8⁺ T-cell abundance has been associated with improved survival rates among OC patients⁹. However, despite the immunogenicity of OC, clinical trial results suggest that OC patients may not benefit from ICI therapy¹⁰. This ineffectiveness could be attributed to the highly immunosuppressive nature of the tumor microenvironment (TME), low mutational burden, and limited T-cell infiltration in these patients^{11,12}. Therefore, there is a pressing need for additional therapeutic strategies to effectively treat these individuals. To address the issue of low response rates, it is crucial to understand the complexities of the immunological response. This understanding will facilitate the identification of novel combination immunotherapy regimens and predictive biomarkers for treatment effectiveness, thereby enabling personalized immunotherapy through patient stratification.

¹Department of Obstetrics and Gynecology, Asan Medical Center, University of Ulsan College of Medicine, 88, Olympic-ro 43-gil, Songpa-gu, Seoul 05505, Republic of Korea. ²Asan Preclinical Evaluation Center for Cancer TherapeutiX, Asan Medical Center, Seoul, Republic of Korea. ³Department of Radiation Oncology, Asan Medical Center, University of Ulsan College of Medicine, Seoul, Republic of Korea. email: swhlee@amc.seoul.kr

The development of new immunotherapy strategies for OC, given its tumor heterogeneity, is hindered by the lack of readily available, high-precision preclinical tumor models. The use of *in vivo* preclinical models is essential for determining the efficacy of potential drug candidates before their introduction into clinical trials. Syngeneic models, such as the widely used ID8 orthotopic murine model and its genetically modified variants, have been extensively used to study the role of the immune system in ovarian cancer progression and to analyze therapeutic responses^{13–15}. However, these syngeneic models do not accurately represent human disease. This discrepancy becomes problematic when the therapeutic agent under investigation is responsive only to human isoforms, or when the expression levels of the targets of interest vary between human and mouse immune cell subsets. Therefore, there is a need for comprehensively characterized mouse models with a functionally intact humanized immune system. These models are crucial for assessing immunotherapy agents and understanding the underlying mechanisms contributing to the lack of response to immunotherapy.

Humanized (Hu) mouse models, featuring cell line-derived xenograft (CDX) or patient-derived xenograft (PDX) tumors, have been utilized to study the efficacy of PD-1/PD-L1 immune checkpoint inhibitors (ICIs) across various cancer types. These models are established in immunodeficient mice engrafted with CD34⁺ hematopoietic stem cells (HSCs), allowing for the characterization of distinct circulating and tumor-infiltrating immune cell profiles, as well as the observation of diverse anti-tumor efficacy of PD-1/PD-L1 ICIs^{16–18}. Specifically for OC research, intraperitoneal and subcutaneous xenograft models of defined OC cell lines and patient-derived cells have been employed. These models are used to study the effect of immunotherapy agents in Hu-mice, as well as cytotoxic therapeutics and targeted agents in immunocompromised mice, such as nude and NOD/SCID/IL2rgnull (NSG) mice^{19–22}.

In this study, we established and characterized two intraperitoneal CDX models of OC in Hu-mice engrafted with CD34⁺ HSCs, and evaluated their responsiveness to PD-1 blockade. Our investigation centered on changes in the TME during anti-PD-1 treatment for OC. To this end, we examined the cellular and molecular characteristics of xenografts in CD34⁺ Hu-mice undergoing PD-1 blockade treatment.

Materials and methods

Cell lines

The SKOV-3-Luc-D3 cell line was purchased from Caliper Life Sciences (Hopkinton, MA, USA). The OVCAR-3 cell line was obtained from the Korean Cell Line Bank (KCLB, Seoul, Korea) and transfected with the pGL3 vector (Madison, WI, USA) containing the firefly luciferase gene. Cell lines were grown in RPMI-1640 medium supplemented with 10% fetal bovine serum and 1% antibiotic-antimycotic solution at 37 °C. The authentication of the cell lines was conducted using short-tandem repeat (STR) profiling within the last 3 years. The presence of Mycoplasma contamination was assessed using the MycoAlert[™] PLUS detection kit (Lonza, Basel, Switzerland). All experiments were performed with mycoplasma-free cells.

Mice

For this study, 20-weeks-old female NOD.Cg-Prkdc^{scid}Il2rg^{tm1Wjl}/SzJ (NSG) and NOD/ShiLtJ-Prkdc^{em1AMC} Il2rg^{em1AMC} (NSGA) mice engrafted with human CD34⁺ HSCs were obtained from Jackson Laboratory (Bar Harbor, ME, USA) and JA BIO (Suwon, Korea). When the mice were 3–4 weeks old, they were exposed to whole-body irradiation. Subsequently, each mouse received an intravenous injection of 1 × 10⁵ CD34⁺ HSCs. All mice were housed in a specific pathogen-free environment in the Disease Animal Research Center's experimental facility at Asan Medical Center (Seoul, Korea). They were provided with sterilized food and water, available ad libitum. All animal experiments were approved by the Institutional Animal Care and Use Committee (IACUC) of the Asan Institute for Life Sciences at the Asan Medical Center, and the studies were conducted in accordance with the approved guidelines and regulations (approval ID: 2022-12-233). Furthermore, this study is reported in accordance with the applicable ARRIVE guidelines.

In vivo experiments

In the intraperitoneal xenograft model, 1 × 10⁷ SKOV-3 Luc and OVCAR-3 Luc cells, mixed with 50% matrigel, were injected into the peritoneal cavity of humanized NSG or NSGA mice 17–18 weeks post-transplantation of CD34⁺ cells. Tumor development was tracked on a weekly basis using bioluminescence imaging. For this, mice were anesthetized with isoflurane, followed by an intraperitoneal injection of D-luciferin solution (150 mg/kg). Imaging was conducted using an IVIS Spectrum system 10 min post-injection. The bioluminescent signal was quantified using Living Image 3.1 (Caliper Life Sciences, Hopkinton, MA, USA). To investigate the sensitivity to PD-1 blockade, mice were imaged using the IVIS system two weeks post-inoculation of SKOV-3 Luc cells to confirm tumor development. They were then randomly divided into two groups of eight: a PBS control group, and a group treated with Pembrolizumab. PBS and pembrolizumab (10 mg/kg) were administered intraperitoneally, twice a week for three weeks. Tumor growth was monitored using the IVIS imaging system. A week after the final treatment, the mice were euthanized by CO₂ gas, and their tumor tissues were collected for further analysis. Tumor volumes were determined based solely on the tissue where the tumor was identified through histological analysis. Statistical analyses were conducted on these tumor volumes.

Histological analysis, immunohistochemistry, and immunofluorescence microscopy

After the final *in vivo* optical imaging, all tumor-bearing mice were humanely euthanized in accordance with our experimental protocol. The tumor tissues located in the peritoneal cavity were isolated, fixed, and embedded in paraffin for subsequent analysis, and the corresponding tissue sections were stained with hematoxylin and eosin (H&E). For the processes of immunohistochemistry (IHC) and immunofluorescence (IF) staining, antigen retrieval was performed by heating the paraffin-embedded tissue sections in Tris-EDTA buffer (Vector

Laboratories, Newark, CA, USA). Subsequently, the slides were blocked using 2.5% normal goat serum blocking solution (Vector Laboratories, Newark, CA, USA) for 30 min at room temperature (RT). Endogenous peroxidase activity, relevant for IHC, was inhibited using BLOXALL Endogenous blocking solution (Vector Laboratories, Newark, CA, USA). The tissue sections were then stained overnight at 4 °C with primary antibodies against anti-CD3 (EP449E, Abcam, Cambridge, MA, USA), anti-CD4 (AF-379-NA, R&D Systems, Minneapolis, MN, USA), anti-CD8 (4B11, Novus Biologicals, Centennial, CO, USA), and anti-PD-L1 (E1L3N, Cell Signaling, Danvers, MA, USA). These sections were subsequently incubated for 2 h at RT with secondary antibodies. For IHC, biotinylated mouse or rabbit IgG (Abcam, Cambridge, MA, USA) were used, while for IF, mouse IgG tagged with Alexa Flour 488 and goat IgG tagged with Alexa Flour 555 (Invitrogen, Carlsbad, CA, USA) were applied. Further, IHC slides were subjected to a 30-min incubation at RT with ABC reagents (Vector Laboratories, Newark, CA, USA), followed by 10-min staining with DAB, and counterstaining with 1% methyl green. Finally, the sections were embedded with mounting medium, applicable for IHC and IF (with DAPI), respectively. The images of H&E and IHC were acquired using the BX53 microscopy (Olympus, Tokyo, Japan) and VS200 digital slide scanner (Olympus, Tokyo, Japan). In addition, the IF images were captured using an LSM 710 confocal microscope (Carl Zeiss, Oberkochen, Germany).

Flow cytometry

Tumor tissues were dissociated for 1 h at 37 °C using RPMI with 10% FBS, 1 mg/ml type IV collagenase (Sigma-Aldrich, Saint Louis, MO, USA), 0.2 mg/ml hyaluronidase (Sigma-Aldrich, Saint Louis, MO, USA), and 0.1 mg/ml DNase I (Roche, Basel, Switzerland). Single cells were mechanically isolated from lymph nodes and spleen tissues using cell strainers and syringe plungers. Peripheral blood mononuclear cells (PBMCs) were separated using the Histopaque-1077 (Sigma-Aldrich, Saint Louis, MO, USA) gradient method. The cell surface was blocked with an Fc-block antibody (BD Biosciences, Franklin Lakes, NJ, USA) and subsequently stained with respective fluorochrome-conjugated antibodies for 30 min. The antibodies used for analysis were from Biolegend (San Diego, CA, USA) or Invitrogen (Carlsbad, CA, USA), including anti-CD45 (304029, HI30 clone), anti-CD3 (300406, UCHT1 clone), anti-CD4 (300514, RPA-T4 clone), anti-CD8 (344710, SK1 clone), anti-CD56 (318318, HCD56 clone), anti-CD11b (301306, ICRF44 clone), anti-CD19 (302218, HIB19 clone), and anti-PD-1 (12-9969-42, MIH clone). PE Mouse IgG1 kappa isotype control from BD Biosciences (Franklin Lakes, NJ, USA) was used in parallel to PD-1. Dead cells were excluded with a Live/Dead Cell Stain kit (Invitrogen, Carlsbad, CA, USA). Single cells were identified by FACS Canto II (BD Biosciences, Franklin Lakes, NJ, USA), and the data were analyzed with FlowJo software (TreeStar, Woodburn, OR, USA). The gating strategy used in the flow cytometry analysis is depicted in Supplementary Fig. 7.

RNA-seq analysis

Total RNA was isolated from the tumor tissues of SKOV-3 Luc xenograft in Hu-mice treated with either PBS or pembrolizumab. The isolation was performed using the RNeasy Mini Kit (Qiagen, Hilden, Germany). The tumor tissues used were from two mice in the PBS group and three mice in the pembrolizumab-treated group. A library was prepared with 100 ng of total RNA for each sample using the TruSeq RNA Access library prep kit (Illumina, San Diego, CA, USA). Subsequently, the indexed libraries were submitted to an Illumina NovaSeq (Illumina, San Diego, CA, USA), and the paired-end (2×100 bp) sequencing was performed by Macrogen.

Data processing and differential gene expression analysis

Trimmomatic v0.38 was utilized to remove adapter sequences and trim bases with subpar quality before analysis. Following this, the refined reads were aligned to the Homo sapiens (GRCh38) genome using HISAT v2.1.0²³, based on the HISAT and Bowtie2 implementations. The reference genome sequence and gene annotation data were obtained from the NCBI Genome assembly and the NCBI RefSeq database, respectively.

The aligned data, in SAM file format, were sorted and indexed using SAMtools v1.9. StringTie v2.1.3b was employed for the assembly and quantification of transcripts after alignment^{24,25}. Quantification was conducted at both gene and transcript levels, with results presented as raw read count, FPKM (Fragments Per Kilobase of transcript per Million mapped reads), and TPM (Transcripts Per Million).

Statistical analyses of differential gene expression were performed with edgeR exactTest, using raw counts as input²⁶. The results from the exactTest provided both fold change and p-values. These p-values were subsequently adjusted using the Benjamini-Hochberg algorithm to control the false discovery rate (FDR). The list of significant genes was then filtered according to the criteria of $|fold\ change| \geq 2$ and raw p-value < 0.05 . Hierarchical clustering was performed on rlog transformed values for the significant genes, with parameters set to Euclidean distance for the distance metric and complete for the linkage method.

Gene set enrichment analysis (GSEA)

GSEA of RNA-seq data was conducted to investigate potential mechanisms underlying resistance to PD-1 blockade in OC. The reference gene sets were obtained from the Molecular Signatures Database (MSigDB). This included the following categories: Hallmark (H), Curated (C2), Ontology (C5), Immunologic Signature (C7), and Cell Type Signature (C8) gene sets²⁷. Significance was determined by nominal p-values less than 0.05 and a false discovery rate (FDR) less than 0.25.

CIBERSORTx analysis

The relative proportions of 22 types of tumor-infiltrating immune cells were analyzed using the CIBERSORTx algorithm, in conjunction with the LM22 matrix^{28,29}. The normalized RNA-seq gene expression file of the tumors in Hu-mice was uploaded to the CIBERSORTx portal (<https://cibersortx.stanford.edu/>) as a mixture file. The

LM22 gene signature was then employed to run the algorithm, using 100 permutations. The resulting relative fractions of the 22 immune cell types were visualized in a heatmap and a bar chart.

Statistics

Statistical analysis was performed using GraphPad Prism software. Either a Student's t-test or analysis of variance (ANOVA) was used for comparison.

Results

Tumor growth of ovarian cancer cells in Hu-mice following intraperitoneal injection.

To confirm the establishment of the intraperitoneal xenograft model of OC in Hu-mice, we intraperitoneally inoculated Hu-mice with two luciferase-expressing cell lines (the highly invasive SKOV-3 Luc and the less invasive OVCAR-3 Luc³⁰) after humanization via engraftment of CD34⁺ cells. We then monitored the weekly tumor growth progression over time using bioluminescence imaging (BLI) (Fig. 1A). Both models showed growth in Hu-mice, with SKOV-3 Luc demonstrating more aggressive growth than OVCAR-3 Luc (Fig. 1B–E, Supplementary Fig. 1).

All mice in the SKOV-3 Luc model with increasing BLI exhibited solid tumor tissues in the intraperitoneal cavity (Fig. 1F). This model showed a tumor take rate of 50.0% and a rate of ascites formation at 25.0% within 7 weeks. In contrast, mice in the OVCAR-3 Luc model with an increase in BLI developed milky ascitic fluid,

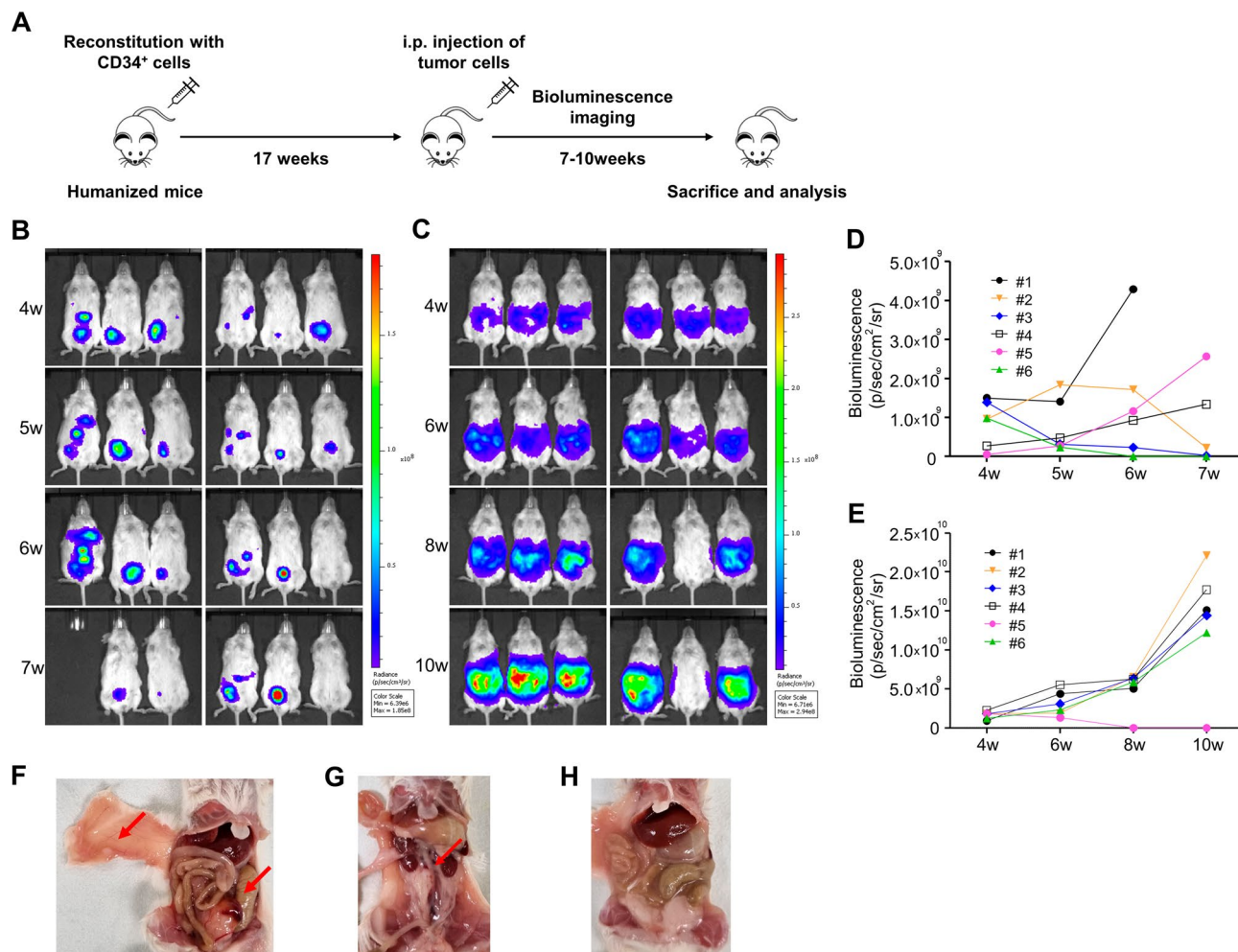


Figure 1. Growth of ovarian cancer cells as intraperitoneal xenografts in Hu-mice. (A) A schematic overview of the experimental setup for generating intraperitoneal ovarian cancer xenograft model in Hu-mice. Briefly, 1×10^7 SKOV-3 Luc and OVCAR-3 Luc cells were injected intraperitoneally into Hu-mice, respectively, at 17 weeks after transplantation of human CD34⁺ cells. In vivo bioluminescence images (BLI) were repeatedly obtained until 7–10 weeks after IP injection of (B,D) SKOV-3 Luc and (C,E) OVCAR-3 Luc cells. Increase in BLI intensity of photons over time demonstrated growth of tumors. After 7–10 weeks post-transplant, (F) representative images of tumors (red arrow) from Hu-mice injected with SKOV-3 Luc and (G) OVCAR-3 Luc cells. (H) Representative image of milky ascites formation in OVCAR-3 Luc model.

showing an ascites formation rate of 83.3% within 10 weeks. However, these mice had a low tumor take rate of only 8.3% (Fig. 1G,H).

Immunological characterization of ovarian xenograft tumors in Hu-mice

Tumor-infiltrating immune cells, such as lymphocytes and myeloid cells, along with the expression of programmed cell death ligand 1 (PD-L1), have been associated with the response to PD-1/PD-L1 ICI treatment³¹. We performed colorimetric immunostaining to identify the presence of TILs and PD-L1 expression in the tumors of Hu-mice. We observed CD3⁺, CD4⁺, and CD8⁺ human T cells within both SKOV-3 Luc and OVCAR-3 Luc xenografts derived from these Hu-mice (Fig. 2A,B). Additionally, we demonstrated distinct PD-L1 expression on the tumors (Fig. 2C).

Concurrently, flow cytometry analysis revealed the presence of not only human lymphocytes but also myeloid cells within the tumors of SKOV-3 Luc and OVCAR-3 Luc in Hu-mice. More specifically, we observed human CD45⁺ hematopoietic cells, CD4⁺ T cells, CD8⁺ T cells, CD56⁺ NK cells, CD11b⁺ myeloid cells, and CD19⁺ B cells.

The SKOV-3 models presented a range of tumor-infiltrating human CD45⁺ cells, ranging from 6.5 to 44.9%, with an average of 32.7%. Within this CD45⁺ cell population, the frequency of CD4⁺ and CD8⁺ T cells spanned 27.3% to 62.6% and 0.9% to 45.6%, averaging at 43.4% and 30.1%, respectively. Moreover, the prevalence of CD56⁺ cells within CD45⁺ cells varied from 15.9 to 38.1% (mean = 29.0%), and CD11b⁺ cells ranged from 1.4 to 25.7% (mean = 9.7%). In contrast, the average frequency of CD19⁺ B cells was quite low at 2.6%, with a range from 1.2 to 5.9% (Fig. 2D).

In the OVCAR-3 Luc xenograft tumor, the proportion of tumor-infiltrating human CD45⁺ cells was 17.1% of the viable cells within the tumor. Within the CD45⁺ cell subset, the percentages of CD4⁺ and CD8⁺ T cells varied, comprising 46.3% and 34.2% of human CD45⁺ cells, respectively. Additionally, the frequencies of CD56⁺ cells

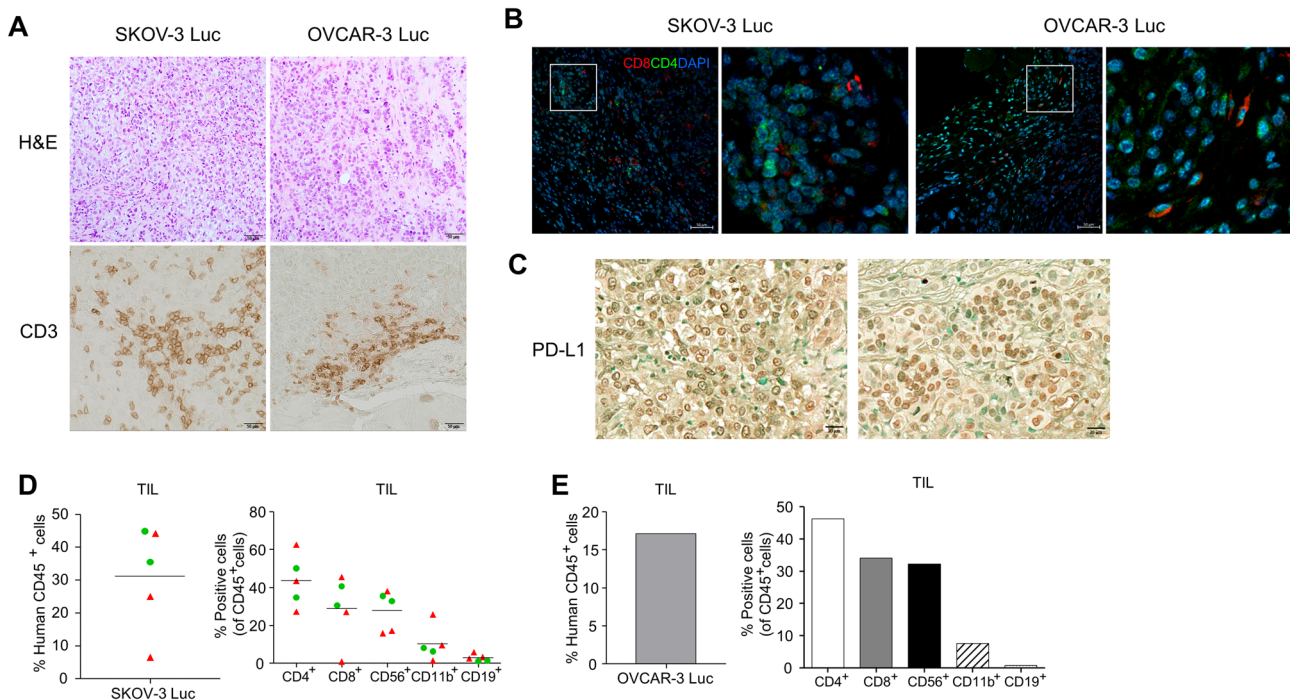


Figure 2. Presence of tumor-infiltrating lymphocytes (TILs) and immunophenotypical characterization of tumors in Hu-mice injected with ovarian cancer cells. The infiltration of human lymphocytes and the immunophenotype within the ovarian xenograft tumors of Hu-mice were determined by colorimetric immunostaining and flow cytometry analysis. Tumor samples were collected from the peritoneal cavity, processed through formalin fixation and paraffin embedding, then sectioned for histologic examination and analysis of immune cells and PD-L1 expression. (A) The tumor characteristics are visualized via hematoxylin and eosin staining (H&E, top panels) and immunohistochemical staining of CD3⁺ T cells (bottom panels) in tumors. (B) Immunofluorescence imaging enabled the detection of CD4⁺ and CD8⁺ T cells by utilizing anti-human CD4 (Green) and CD8 (Red) antibodies. DAPI was used for nuclear staining (Blue). Magnification, $\times 20$; Scale bar, 50 μm . (C) The expression of PD-L1 expression in SKOV-3 Luc (left panel) and OVCAR-3 Luc (right panel) tumors was determined by an immunohistochemical method using the anti-human PD-L1 antibody (Magnification, $\times 20$; Scale bar, 20 μm). Solid tumor tissues from Hu-mice injected with ovarian cancer cells were dissociated into single cells using enzymes and mechanical methods. These collected cells were then labeled with fluorochrome-conjugated anti-human antibodies. The presence and frequency of human CD45⁺ cells, CD4⁺ T cells, CD8⁺ T cells, CD56⁺ natural killer (NK) cells, CD11b⁺ myeloid cells, and CD19⁺ B cells within the tumor tissues of (D) SKOV-3 Luc ($n=5$) and (E) OVCAR-3 Luc ($n=1$) models were evaluated using flow cytometry. The first batch was denoted by red triangles, and the second batch was denoted by green circles.

and CD11b⁺ cells were observed at 32.3% and 7.6%, respectively. As with the SKOV-3 Luc model, CD19⁺ B cells in the OVCAR-3 Luc tumor remained extremely low, accounting for up to only 0.7% (Fig. 2E).

Immunophenotyping of draining lymph node, peripheral blood, and spleen in ovarian tumor-bearing Hu-mice

We next conducted an immune profiling analysis of tumor-draining lymph nodes (DLNs), peripheral blood samples, and spleens from Hu-mice injected with SKOV-3 Luc and OVCAR-3 Luc cells. Lymph nodes in NSG mice are notably underdeveloped, as evidenced by their remarkably small size, which in some cases renders them nearly undetectable³². However, we successfully obtained a lymph node of sufficient size located near the SKOV-3 Luc and OVCAR-3 Luc tumor tissues in Hu-mice.

DLNs from the SKOV-3 Luc model revealed a significant proportion of human CD45⁺ cells, demonstrating an immune cell subset pattern similar to that of the tumors, with the exception of CD19⁺ B cells (Fig. 3A,B). In the blood and spleen, more than 40% of the human CD45⁺ cell populations were detected (Fig. 3C). The proportion of CD19⁺ B cells within the CD45⁺ cell population ranged from 1.0 to 27.4% (mean = 13.1%) and from 2.9 to 51.5% (mean = 25.7%) in the blood and spleen, respectively. These values were notably higher than those observed in tumors, in contrast to the frequencies of CD4⁺, CD8⁺, CD56⁺, and CD11b⁺ cell subsets, which exhibited a similar pattern (Fig. 3D–H).

The DLN of the OVCAR-3 Luc model also displayed a very high proportion of human CD45⁺ cells, reaching up to 96.3% (Fig. 3I). The immune cell phenotypes of the DLN, blood, and spleen were consistent with those of the SKOV-3 Luc model, showing relatively higher frequencies of B cells than the tumor tissue (Fig. 3J–P).

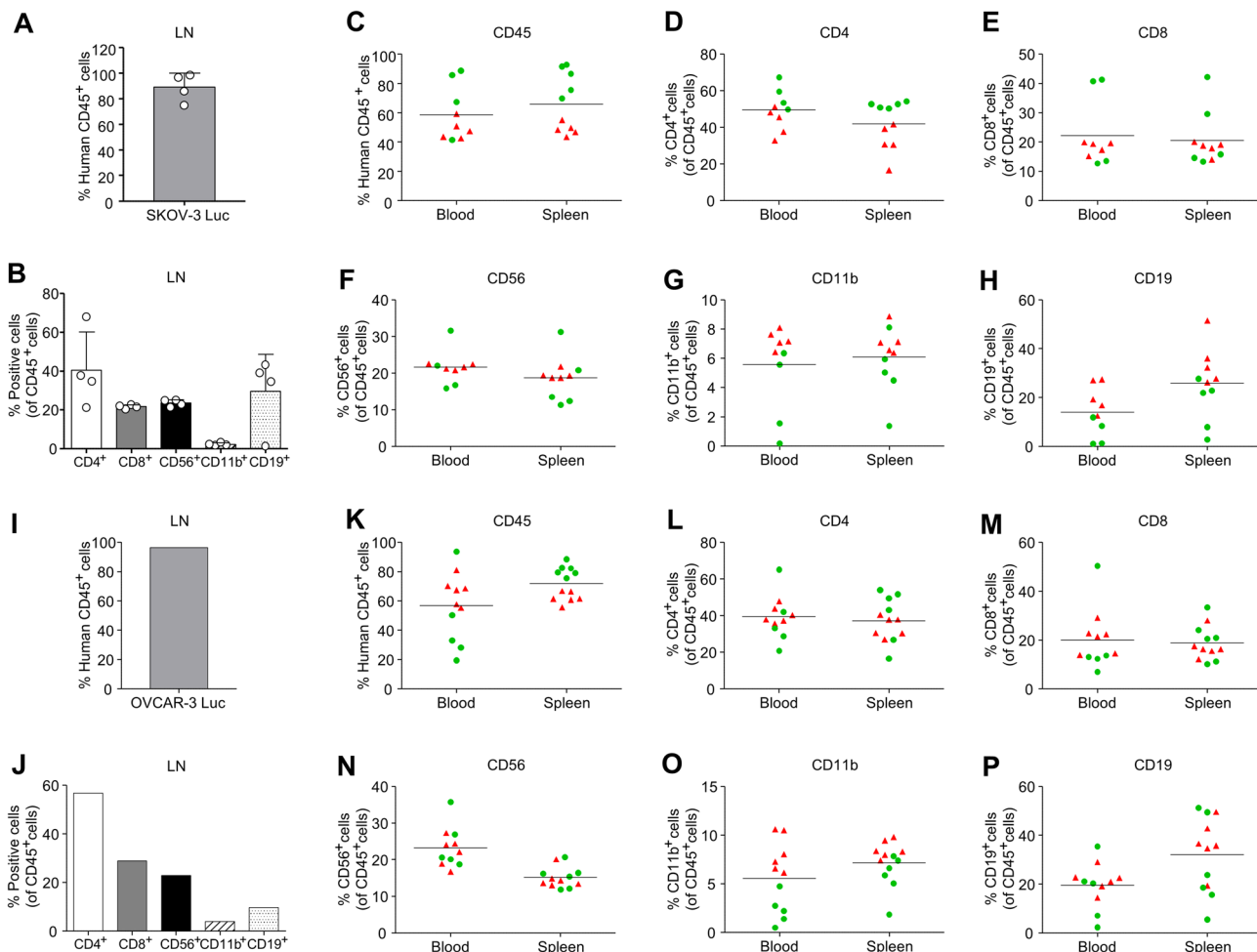


Figure 3. Immunophenotypical characterization of draining lymph node, blood and spleen in Hu-mice injected with ovarian cancer cells. Immunophenotyping for the prevalence of human immune cells within the draining lymph node, blood, and spleen of Hu-mice injected with (A–H) SKOV-3 Luc and (I–P) OVCAR-3 Luc cells. Flow cytometry analysis of human CD45⁺ cells, CD4⁺ T cells, CD8⁺ T cells, CD56⁺ natural killer (NK) cells, CD11b⁺ myeloid cells, and CD19⁺ B cells are shown. Data are from two independent experiments. The bar graphs for the lymph node in the OVCAR-3 Luc model represent data from a single tissue sample (I,J). The first batch was denoted by red triangles, and the second batch was denoted by green circles.

Refractory response to pembrolizumab and characterization of human lymphocytes in SKOV-3 Luc tumor-bearing Hu-mice

Recently, numerous clinical trials have been conducted to incorporate ICIs targeting PD-1/PD-L1 into the treatment regimen for OC³³. To investigate the response and underlying mechanisms related to blocking the interaction between PD-1 and PD-L1 in OC, we administered pembrolizumab, an anti-PD-1 antibody, to the intraperitoneal SKOV-3 xenograft model in CD34⁺ Hu-mice. Previous research has shown the crystallizable fragment (Fc) receptor engagement on tumor-associated macrophages (TAMs) by anti-PD-1 induces tumor progression³⁴. In our study, we opted to administer PBS, which minimizes its impact on tumor formation and growth, to the control mice instead of an isotype antibody, aiming to confirm the reproducibility of the SKOV-3 Luc model in Hu-mice.

The development of visible SKOV-3 Luc tumors was monitored for two weeks using BLI. Subsequently, the tumor-bearing Hu-mice were randomly divided into two groups: PBS control and pembrolizumab. These mice were then treated for three weeks either with PBS or pembrolizumab, depending on their assigned group. We observed that the body weight of the mice remained relatively stable throughout the treatment (Supplementary Fig. 2). A comparison of tumor growth revealed no significant difference between the control and pembrolizumab groups during the treatment period (Fig. 4A–D). We then determined the histopathological attributes of the tumor tissues, which were excised from the peritoneal cavity of the Hu-mice (Supplementary Fig. 3A,B). The volume of these tumors was calculated by selectively choosing and measuring only the distinct tumor tissues. Consistently, no substantial differences in tumor volumes were found between the two groups, suggesting that the intraperitoneal SKOV-3 Luc xenograft Hu-mouse model exhibited a refractory response to pembrolizumab treatment (Fig. 4E,F).

To assess the activity of pembrolizumab, a drug that binds to and saturates PD-1, we used flow cytometry to quantify human PD-1⁺ lymphocytes, including CD4⁺ T cells, CD8⁺ T cells, and CD19⁺ B cells. Previous studies have shown that depletion of human PD-1⁺ cells can be achieved using pembrolizumab or nivolumab in Hu-mice xenograft models^{35,36}. We found a significant reduction in the abundance of PD-1⁺ lymphocytes in the peripheral blood of Hu-mice treated with pembrolizumab compared to the PBS control group (Fig. 4G). Additionally, it has been reported that patients with OC exhibit a higher frequency of PD-1⁺ CD8⁺ T cells compared to healthy donors³⁷. Analysis of the frequency of PD-1⁺ lymphocytes revealed a higher abundance of both CD8⁺ and CD4⁺ T cells in SKOV-3 Luc tumor-bearing Hu-mice compared to mice without detectable BLI and tumor growth. In contrast, the frequency of CD19⁺ B cells was lower in tumor-bearing mice. The increased prevalence of these T cells is consistent with a higher frequency of PD-1⁺ T cells. However, no observable difference in the frequency of PD-1⁺ B cells was found (Fig. 4H, Supplementary Fig. 4).

Composition of immune cells in tumor tissues of pembrolizumab-unresponsive Hu-mice

To investigate the changes in the TME of unresponsive SKOV-3 Luc-derived tumors treated with pembrolizumab in Hu-mice, we examined and compared the transcriptomes of these tumors with those of the PBS control group. We identified 2,324 differentially expressed genes (DEGs) with $|log_2 \text{ fold change (FC)}| > 2$ and $p < 0.05$, as illustrated in the volcano plot in Fig. 5A. Among these DEGs, 814 were upregulated and 1,510 downregulated in tumors of Hu-mice treated with pembrolizumab.

To further assess the similarity of gene expression patterns between the tumor samples, we employed heatmap-based hierarchical clustering using Euclidean distance and complete-linkage methods (Fig. 5B). Additionally, we utilized CIBERSORTx analysis along with the LM22 signature matrix to examine the relative proportions of different immune cell subpopulations in the RNA-seq data. This digital cytometry method elucidates the proportions of 22 distinct tumor-infiltrating immune cell subtypes in SKOV-3 Luc tumors of Hu-mice that were nonresponsive to pembrolizumab and subsequently compared these findings with PBS control mice (Fig. 5C, Supplementary Fig. 5).

Upon analysis, macrophage fractions were found to be highly abundant within SKOV-3 Luc tumors from Hu-mice, consistent with previously reported CIBERSORT results from the RNA-seq data of The Cancer Genome Atlas (TCGA) for OC³⁸. Moreover, pembrolizumab-refractory xenograft tumors exhibited reduced fractions of CD8⁺ T-cells, memory B cells, and plasma cells, as well as increased proportions of naïve M0 macrophages and activated mast cells, compared to PBS control tumor tissues.

Identifying gene signatures associated with unresponsive anti-PD-1 treatment in SKOV-3 Luc xenografts of Hu-mice

We performed a gene set enrichment analysis (GSEA) on the RNA-seq data from SKOV-3 Luc xenografts in Hu-mice to examine the molecular profile of cancer immunity associated with resistance to anti-PD-1 therapy. Remarkably, we found 39 significantly enriched gene sets in pembrolizumab-nonresponsive tumors that were upregulated compared to the PBS control group (Fig. 6A). The differentially expressed genes (DEGs) within these sets were predominantly enriched in RB1 target genes, KLF1 and 3 target genes, genes associated with epithelial-mesenchymal transition (EMT) and fibroblasts, as well as TCF21, MYD88, and SMARCE1 target genes (Supplementary Fig. 6). Furthermore, we identified 4 significantly enriched gene sets among the downregulated DEGs, encompassing interferon-gamma and alpha response (Fig. 6B).

Notably, one of the main gene sets upregulated in pembrolizumab-nonresponsive tumors was found to be the histone deacetylase (HDAC) class I target genes (Fig. 6A,C). Previous studies have revealed the crucial role of HDAC in cancer immunotherapy. HDAC inhibitors are currently under active clinical examination and are being combined with immunotherapy for solid tumors, a strategy aimed at amplifying therapeutic responses³⁹.

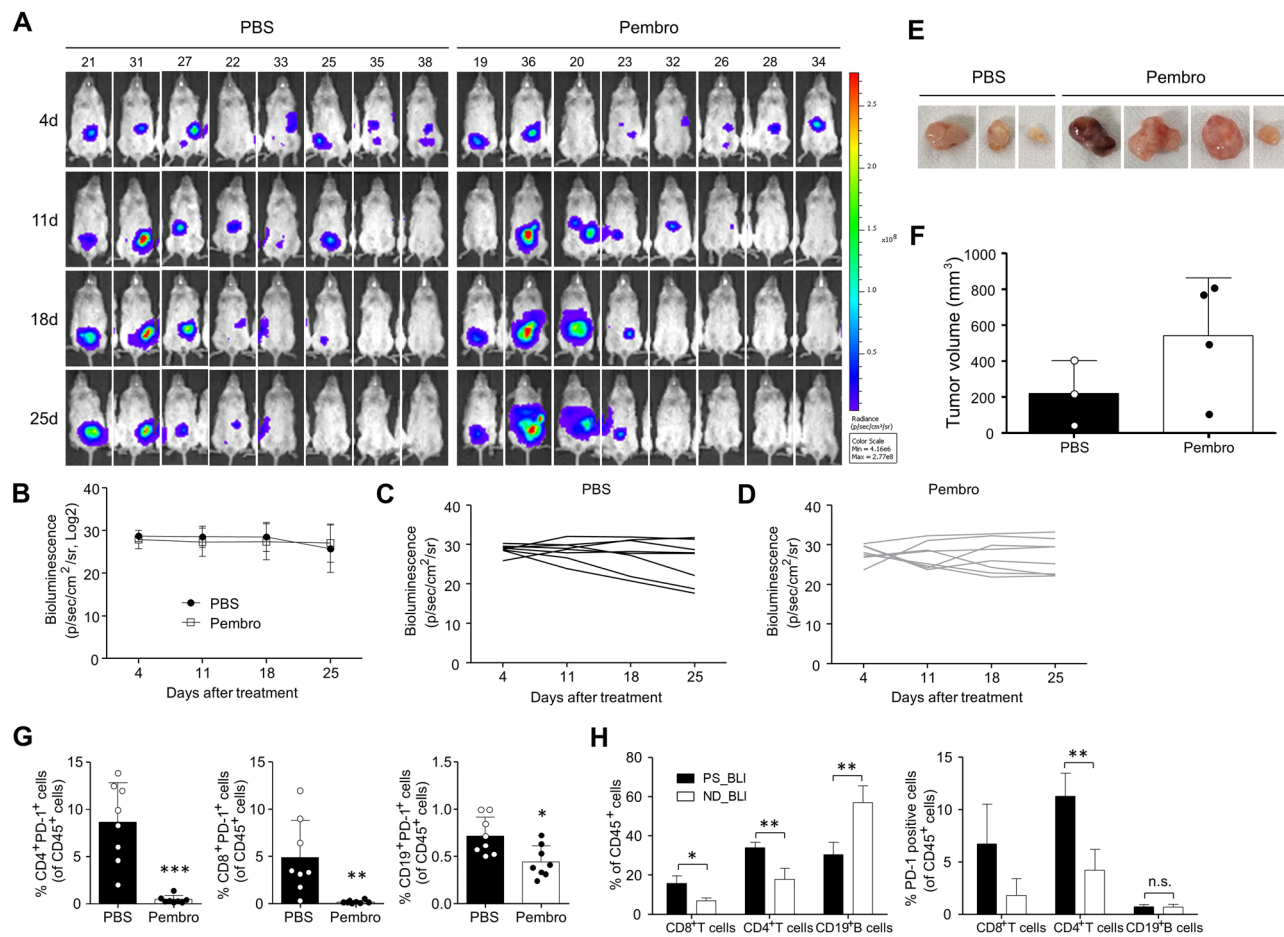


Figure 4. Refractory response to anti-PD-1 treatment and characterization of human lymphocytes in SKOV-3 Luc tumor-bearing Hu-mice. The sensitivity of the Hu-mice ovarian xenograft model to PD-1 blockade was investigated using SKOV-3 Luc cells, which were inoculated intraperitoneally in Hu-mice. The treatment commenced two weeks post-inoculation of cancer cells, with either a PBS control or a twice-weekly intraperitoneal dose of 10 mg/kg pembrolizumab for three weeks. (A) The BLI signal was measured at four distinct time points: 4 days, 11 days, 18 days, and 25 days post-treatment administration. (B) The intensity of BLI was quantified in (C) PBS control and (D) pembrolizumab groups. (E,F) SKOV-3 Luc cell line-derived tumors were dissected from the peritoneal cavity of Hu-mice and their volumes were subsequently measured. The effectiveness of pembrolizumab was confirmed through the analysis of target PD-1⁺ lymphocytes in Hu-mice SKOV-3 Luc xenograft model. (G,H) Frequencies of human CD4⁺ T cells, CD8⁺ T cells, and CD19⁺ B cells expressing PD-1 in the blood were evaluated using flow cytometry (Supplementary Fig. 7B). Data from mice in the PBS group were then analyzed and compared between two sets: those categorized under ND_BLI and those under PS_BLI. The ND_BLI refers to instances where no BLI was detected at the end of the experiment. In contrast, PS_BLI represents instances where there was either a steady or progressively increasing exposure to BLI at the end of the experiment. P values were calculated using unpaired t-test (*P<0.05, **P<0.01, ***P<0.001).

Discussion

Preclinical studies using animal models that accurately mimic the human immune system are crucial in elucidating the potential clinical outcomes and underlying mechanisms of immuno-oncology (IO) drugs^{40,41}. These studies aid in understanding the TME and assessing the prognostic significance of IO drugs, such as PD-1/PD-L1 ICIs, which have shown limited efficacy in treating OC^{17,36,42}. In this study, we demonstrated the tumor growth of two intraperitoneal OC xenografts in Hu-mouse models and characterized their morphological and immunophenotypic features. Furthermore, we identified several pivotal genes and biological pathways in the TME of OC that could serve as potential therapeutic targets for improving the efficacy of anti-PD-1 treatment. This was achieved using SKOV-3 Luc humanized xenografts that showed non-responsiveness to pembrolizumab.

In recent years, significant progress has been made in the development and application of Hu-mouse xenograft models. The most common methods for testing cancer immunotherapy involve the subcutaneous implantation of established cell lines and patient-derived tissues^{16,18,36,43}. However, these models may not always accurately reflect the characteristics of the primary tumor, as they lack interaction with the TME, and do not provide the conditions necessary for metastasis. Orthotopic xenografts can offer a more accurate representation of the metastatic behavior of tumors and their TME^{44,45}. Previous studies have explored the development of orthotopic xenograft

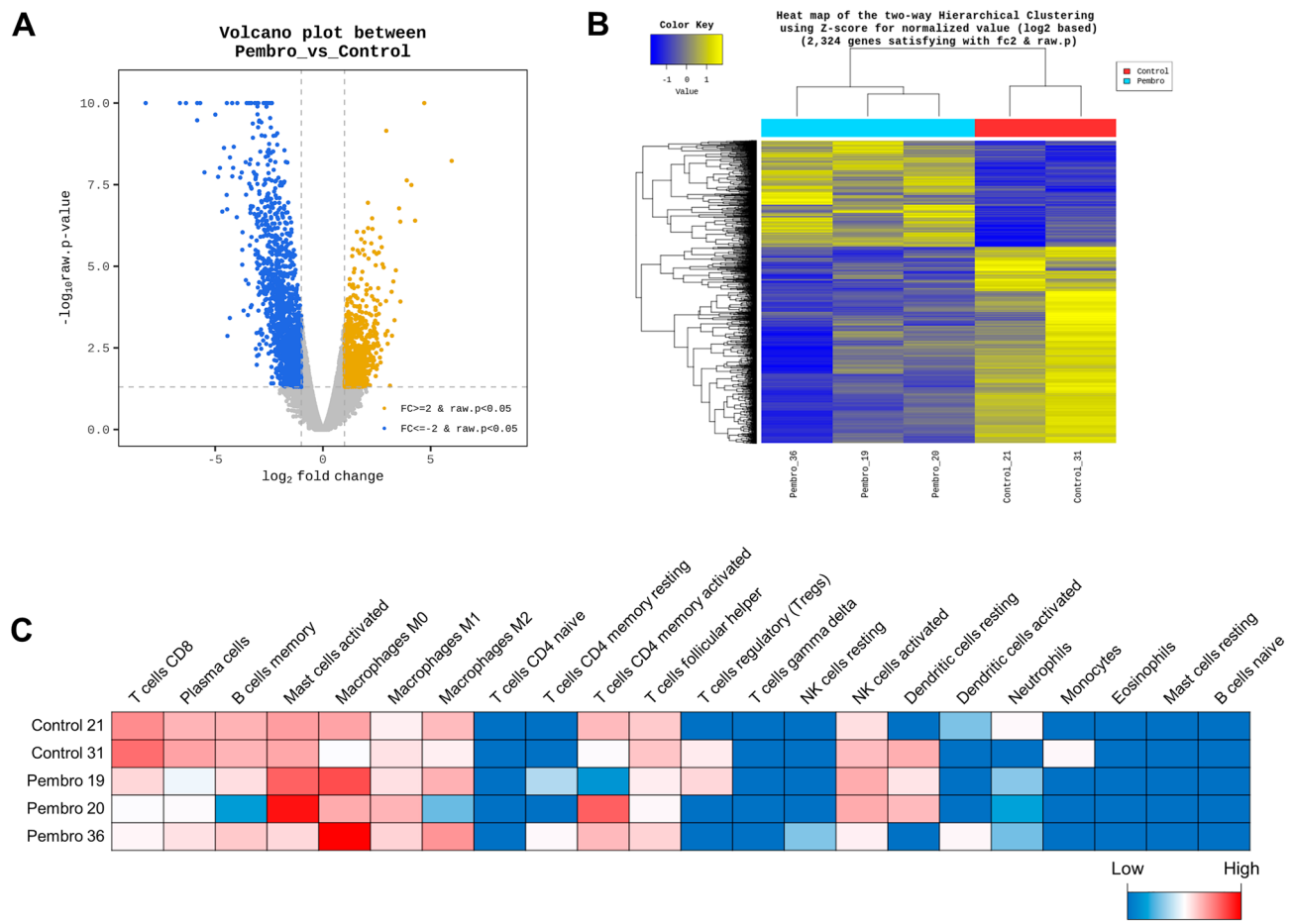


Figure 5. Transcriptome profiles and CIBERSORTx analysis of RNA sequencing data in tumor tissues of pembrolizumab non-responsive and PBS-controlled Hu-mice. The RNA-seq analysis examined the differences in gene expression within the TME of SKOV-3 Luc tumors unresponsive to pembrolizumab treatment, compared to the PBS control group. (A,B) Volcano plots and heatmap showing differentially expressed genes (DEGs, 814 upregulated and 1,510 downregulated genes). (A) Y-axis of volcano plots displays the p-value (-log 10) of the mean expression, and the x-axis shows the log twofold change value. Gold (upregulated genes, log2FC > 2) and Blue (downregulated genes, log2FC < -2) dots indicate significant DEGs ($p < 0.05$). (B) The genes (rows) and samples (columns) are clustered using Euclidean distance and complete-linkage methods. The heatmap displays z-scores for log2-normalized read counts that are statistically significant ($|log2(FC)| > 2$, $p < 0.05$). Yellow color indicates higher gene expression and blue color indicates lower gene expression. (C) The 22 subtypes of tumor-infiltrating immune cells are quantified using CIBERSORTx analysis. The heatmap visually represents the distribution of immune cell compositions in SKOV-3 Luc xenograft tumors, comparing those treated with PBS and Pembrolizumab.

models in Hu-mice, using luciferase-positive human pancreatic and osteosarcoma cells^{46,47}. The orthotopic OC xenograft model in Hu-mice, using the OV-90 luciferase cell line and PDX cells, was initially employed to verify the response to nivolumab¹⁹. As an alternative approach that avoids surgical incisions and offers simplicity, we intraperitoneally injected the luciferase-expressing SKOV-3 and OVCAR-3 cell lines into CD34⁺ Hu-mice. We confirmed tumor formation and progression through *in vivo* BLI (Fig. 1B–E). In Hu-mice, both SKOV-3 Luc and OVCAR-3 Luc intraperitoneal xenograft models were less aggressive and showed a relatively long survival time (more than 6 weeks), consistent with previous studies^{20,48}.

Tumor-infiltrating immune cells play a crucial role in modulating responses to immunotherapy in many solid tumors. The response to anti-PD-1/PD-L1 therapy is positively correlated with the degree of pre-existing TILs, including CD8⁺ T cells expressing PD-L1⁷. Conversely, immunosuppressive immune cells such as TAMs and regulatory T cells (Tregs) have been associated with a poor prognosis in ovarian cancer (OC)^{49–51}. These cells facilitate tumor immune evasion, potentially leading to resistance to PD-1/PD-L1 therapy⁵². In our study, we characterized the profiles of human immune cells within tumors, DLNs, blood, and spleen of Hu-mice. Our observations confirmed the presence of human immune subsets involved in both lymphocytes and myeloid cells, which are responsible for innate and adaptive immune responses. We identified a significant proportion of CD11b⁺ myeloid cells in ovarian xenografts from the peritoneal cavity of Hu-mice. These findings are consistent with other models using Hu-mice, including subcutaneous xenografts for various types of cancer and the orthotopic OC model^{16,19}. Furthermore, our transcriptome data within SKOV-3 Luc tumors of Hu-mice revealed various populations of human immune cells, including T and B lymphocytes, natural killer (NK) cells,

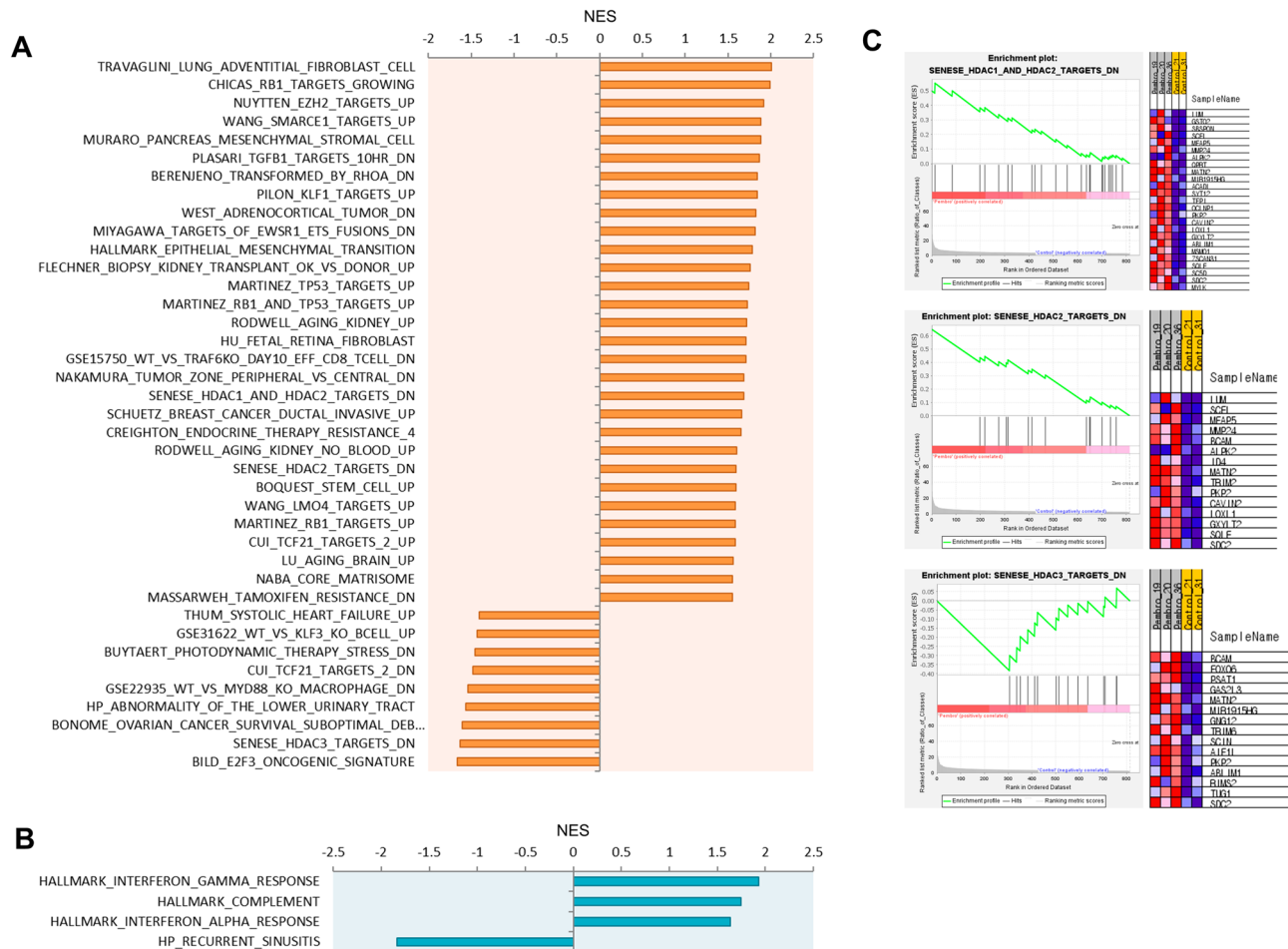


Figure 6. Gene set enrichment analysis (GSEA) results in pembrolizumab refractory xenograft tumors. The gene signatures in pembrolizumab non-responsive SKOV-3 Luc tumors were identified by GSEA. Significantly enriched gene sets ($\text{FDR } q\text{-value} < 0.25$) among (A) upregulated and (B) downregulated genes in the pembrolizumab compared to the control group. (C) Enrichment plots show the genes associated with histone deacetylase (HDAC) targets. All gene sets were selected from the molecular signatures database (MSigDB), specifically categories C2, C5, C7, C8, or H.

M0/M1/M2 macrophages, dendritic cells, neutrophils, and mast cells. Interestingly, this intraperitoneal model displayed a substantial distribution of macrophages within the tumors, in contrast to subcutaneous xenografts where macrophages were found in very low proportions¹⁶. These results are in line with the known characteristics of the TME for patients with OC^{38,50}. Consequently, our model can be utilized to evaluate the anti-tumor efficacy of potential immuno-oncology drug treatments for OC, particularly in the TME where there is a high abundance of macrophages.

Previous studies have reported varying sensitivities in Hu-mice xenograft models exposed to PD-1/PD-L1 ICIs, such as pembrolizumab, nivolumab, and atezolizumab, across different types of cancer^{16,19,35}. In this study, despite the effective blocking of the PD-1 protein on T and B lymphocytes when treated with pembrolizumab (Fig. 4G), the SKOV-3 Luc Hu-mouse model did not show any significant inhibition of tumor growth (Fig. 4A–F). Indeed, in a clinical trial, the objective response rate (ORR) of pembrolizumab as a single-agent treatment was only 8% in patients with advanced OC¹⁰. We observed a reduced presence of CD8⁺ T cells, memory B cells, and plasma cells in SKOV-3 Luc xenografts from pembrolizumab nonresponsive Hu-mice, compared to PBS control mice (Fig. 5C). It has been reported that patients with melanoma and renal cell carcinoma who did not respond to ICIs had a lower frequency of memory B cells and plasma cells in their tumors compared to responders. These B cell subsets were associated with a more favorable response to ICIs, potentially facilitating an enhanced T cell response⁵³. Interestingly, elevated levels of mast cells were observed in SKOV-3 Luc tumors that did not respond to anti-PD-1 treatment (Fig. 5C). Previous research examining the anti-PD-1 response in a melanoma xenograft model using Hu-mice also reported an increase in the prevalence of tumor-infiltrating mast cells following pembrolizumab treatment. This increase is associated with resistance to PD-1 blocking, facilitated by interactions with Treg cells and the subsequent down-modulation of MHC class I¹⁷.

The intraperitoneal CDX Hu-mouse model in our study enabled us to explore potential factors associated with unresponsive anti-PD-1 treatment. Our RNA-seq results identified gene sets linked to anti-PD-1 resistance in OC tumors in Hu-mice treated with pembrolizumab (Fig. 6A,B), with a notable enrichment of HDAC

class I target genes. (Fig. 6C). Expression of Class I HDACs was significantly higher in OC tumors compared to normal ovarian tissues⁵⁴. Given the role of HDACs in regulating gene expression of anti-tumor immune response, their link to tumor resistance to anti-PD-1 therapy suggests a strategy for new therapeutic interventions. HDAC inhibition enhances T-cell mediated anti-tumor immune responses by increasing the presence of tumor-infiltrating CD8⁺ T cells and molecules involved in antigen processing and presentation, while also blocking Treg and myeloid-derived suppressor cells (MDSCs) infiltration⁵⁵. Moreover, it has been reported to induce the M1-like conversion of TAM and to enhance the anticancer effects when combined with PD-1/PD-L1 blockade⁵⁶. Clinical trials are currently underway investigating the safety and efficacy of combinations of HDAC inhibitors and PD-1/PD-L1 ICIs in solid tumors³⁹, suggesting that targeting HDACs could potentially reverse resistance mechanisms to anti-PD-1 treatment.

Additionally, our subsequent GSEA of upregulated DEGs revealed a connection between SKOV-3 Luc tumors refractory to anti-PD-1 therapy and EMT, fibroblast-related signatures, and TCF21 target genes (Supplementary Fig. 6D–H). EMT and cancer-associated fibroblasts (CAFs) are known to play an immunosuppressive role in the TME, contributing to tumor progression and immunotherapy resistance in several cancer types, and a significant correlation exists between EMT-related gene expression and stromal components⁵⁷. The expression of TCF21 influences the state of CAFs. Overexpression of TCF21 affects the protoplasmic properties of fibroblast-activated protein (FAP)-high CAFs, which in turn suppresses OC growth, invasion, and metastasis⁵⁸. Moreover, a study has shown that the mesenchymal subtype, characterized by a high presence of EMT-related gene signatures, has a lower number of intraepithelial CD8⁺ tumor-infiltrating T cells, and is associated with poor prognosis⁵⁹. These characteristics of the subtype were consistent with those found in SKOV-3 Luc tumors in Hu-mice treated with pembrolizumab.

The CD34⁺ implanted Hu-mouse model we employed includes most cellular components of the human immune system. However, functional deficiencies in T cells, B cells, and NK cells have been identified, as previously reported⁶⁰. Additionally, while achieving HLA matching between donor HSCs and tumors poses challenges in simulating fully functional human immune systems, several studies have indicated no significant correlation between the anti-tumor responses of PD-1/PD-L1 ICIs and HLA matching in CD34⁺ Hu-mice^{16,35}.

In the xenograft model, tumor take rate is crucial for experimental reproducibility, and the obtained tumor samples are required for subsequent analyses. In our research, a small sample size could negatively affect the likelihood that our findings accurately represent a genuine effect. The SKOV-3 Luc xenograft model exhibited a moderate tumor take rate, while the OVCAR-3 Luc showed over 80% tumor growth in Hu-mice but had a notably low take rate of visually recognizable tumors. It is suggested that observing solid tumors in the peritoneal cavity using the OVCAR-3 Luc model in Hu-mice may require an extended period. It has been reported that tumor growth was not only restricted in the nasopharyngeal cancer PDX model with a humanized immune system¹⁸, but the CD8⁺ T cells in Hu-mice also inhibited melanoma tumor growth¹⁷. The presence of reconstituted human immune cells may have affected tumor development in our OC models. Surgical transplantation techniques, though more intricate, yielded higher take rates and faster growth compared to intraperitoneal methods⁶¹, suggesting potential for enhancing reproducible tumor formation in future orthotopic OC Hu-mouse models.

Moreover, our transcriptome results provided insights into the key factors associated with unresponsive anti-PD-1/PD-L1 treatment in OC, but our study was limited by a small sample size and the absence of tumor samples from anti-PD-1 responsive mice. To understand the underlying mechanisms more deeply, additional elucidation of functional pathways of pivotal genes through loss- or gain-of-function mutations in vitro and in vivo is necessary. Despite these limitations, our OC CDX model using CD34⁺ Hu-mice may be a viable option for exploring responses to IO drugs targeting human tumor immunity, offering more biological information than clinical trials.

In conclusion, our study with intraperitoneal OC CDX model using CD34⁺ Hu-mice identified potential targets for combined treatment strategies to improve the efficacy of PD-1 blockade in OC. The models we generated using Hu-mice can serve as valuable tools for examining the efficacy of new immunotherapies.

Data availability

All data relevant to the study are included in the article or uploaded as supplementary information. Data are available from the corresponding author. RNA sequencing data generated in this study are available in the GEO database with accession code GSE245913.

Received: 30 January 2024; Accepted: 23 April 2024

Published online: 24 May 2024

References

1. Sung, H. *et al.* Global cancer statistics 2020: GLOBOCAN estimates of incidence and mortality worldwide for 36 cancers in 185 countries. *CA Cancer J. Clin.* **71**, 209–249. <https://doi.org/10.3322/caac.21660> (2021).
2. Orr, B. & Edwards, R. P. Diagnosis and treatment of ovarian cancer. *Hematol. Oncol. Clin. North Am.* **32**, 943–964. <https://doi.org/10.1016/j.hoc.2018.07.010> (2018).
3. Kurnit, K. C., Fleming, G. F. & Lengyel, E. Updates and new options in advanced epithelial ovarian cancer treatment. *Obstet. Gynecol.* **137**, 108–121. <https://doi.org/10.1097/AOG.0000000000004173> (2021).
4. Torre, L. A. *et al.* Ovarian cancer statistics, 2018. *CA Cancer J. Clin.* **68**, 284–296. <https://doi.org/10.3322/caac.21456> (2018).
5. Kirchhamer, N., Trefny, M. P., Auf der Maur, P., Laubli, H. & Zippelius, A. Combination cancer immunotherapies: Emerging treatment strategies adapted to the tumor microenvironment. *Sci. Transl. Med.* **14**, eab03605. <https://doi.org/10.1126/scitranslmed.abo3605> (2022).
6. Yang, L., Ning, Q. & Tang, S. S. Recent advances and next breakthrough in immunotherapy for cancer treatment. *J. Immunol. Res.* **2022**, 8052212. <https://doi.org/10.1155/2022/8052212> (2022).
7. Ribas, A. & Wolchok, J. D. Cancer immunotherapy using checkpoint blockade. *Science* **359**, 1350–1355. <https://doi.org/10.1126/science.aar4060> (2018).

8. Chen, S. *et al.* Response efficacy of PD-1 and PD-L1 inhibitors in clinical trials: A systematic review and meta-analysis. *Front. Oncol.* **11**, 562315. <https://doi.org/10.3389/fonc.2021.562315> (2021).
9. Sato, E. *et al.* Intraepithelial CD8+ tumor-infiltrating lymphocytes and a high CD8+/regulatory T cell ratio are associated with favorable prognosis in ovarian cancer. *Proc. Natl. Acad. Sci. USA* **102**, 18538–18543. <https://doi.org/10.1073/pnas.0509182102> (2005).
10. Zhu, J., Yan, L. & Wang, Q. Efficacy of PD-1/PD-L1 inhibitors in ovarian cancer: A single-arm meta-analysis. *J. Ovarian Res.* **14**, 112. <https://doi.org/10.1186/s13048-021-00862-5> (2021).
11. Yarchaoan, M., Hopkins, A. & Jaffee, E. M. Tumor mutational burden and response rate to PD-1 inhibition. *N. Engl. J. Med.* **377**, 2500–2501. <https://doi.org/10.1056/NEJMcl1713444> (2017).
12. Rodriguez, G. M., Galpin, K. J. C., McCloskey, C. W. & Vanderhyden, B. C. The tumor microenvironment of epithelial ovarian cancer and its influence on response to immunotherapy. *Cancers* <https://doi.org/10.3390/cancers10080242> (2018).
13. Lu, L. *et al.* Combined PD-1 blockade and GITR triggering induce a potent antitumor immunity in murine cancer models and synergizes with chemotherapeutic drugs. *J. Transl. Med.* **12**, 36. <https://doi.org/10.1186/1479-5876-12-36> (2014).
14. Gandham, S. K., Rao, M., Shah, A., Trivedi, M. S. & Amiji, M. M. Combination microRNA-based cellular reprogramming with paclitaxel enhances therapeutic efficacy in a relapsed and multidrug-resistant model of epithelial ovarian cancer. *Mol. Ther. Oncolytics* **25**, 57–68. <https://doi.org/10.1016/j.omto.2022.03.005> (2022).
15. Song, M. *et al.* Tumor derived UBR5 promotes ovarian cancer growth and metastasis through inducing immunosuppressive macrophages. *Nat. Commun.* **11**, 6298. <https://doi.org/10.1038/s41467-020-20140-0> (2020).
16. Rios-Doria, J., Stevens, C., Maddage, C., Lasky, K. & Koblish, H. K. Characterization of human cancer xenografts in humanized mice. *J. Immunother. Cancer* <https://doi.org/10.1136/jitc-2019-000416> (2020).
17. Somasundaram, R. *et al.* Tumor-infiltrating mast cells are associated with resistance to anti-PD-1 therapy. *Nat. Commun.* **12**, 346. <https://doi.org/10.1038/s41467-020-20600-7> (2021).
18. Liu, W. N. *et al.* Establishment and characterization of humanized mouse NPC-PDX model for testing immunotherapy. *Cancers* <https://doi.org/10.3390/cancers12041025> (2020).
19. Kleinmanns, K. *et al.* Humanized ovarian cancer patient-derived xenografts for improved preclinical evaluation of immunotherapies. *Cancers* <https://doi.org/10.3390/cancers14133092> (2022).
20. Reznicek, G. A. *et al.* Establishment of a mouse ovarian cancer and peritoneal metastasis model to study intraperitoneal chemotherapy. *Cancers* <https://doi.org/10.3390/cancers12123818> (2020).
21. Xu, X. *et al.* Anti-miR182 reduces ovarian cancer burden, invasion, and metastasis: An in vivo study in orthotopic xenografts of nude mice. *Mol. Cancer Ther.* **13**, 1729–1739. <https://doi.org/10.1158/1535-7163.MCT-13-0982> (2014).
22. Odunsi, A. *et al.* Fidelity of human ovarian cancer patient-derived xenografts in a partially humanized mouse model for preclinical testing of immunotherapies. *J. Immunother. Cancer* <https://doi.org/10.1136/jitc-2020-001237> (2020).
23. Kim, D., Langmead, B. & Salzberg, S. L. HISAT: A fast spliced aligner with low memory requirements. *Nat. Methods* **12**, 357–360. <https://doi.org/10.1038/nmeth.3317> (2015).
24. Pertea, M. *et al.* StringTie enables improved reconstruction of a transcriptome from RNA-seq reads. *Nat. Biotechnol.* **33**, 290–295. <https://doi.org/10.1038/nbt.3122> (2015).
25. Pertea, M., Kim, D., Pertea, G. M., Leek, J. T. & Salzberg, S. L. Transcript-level expression analysis of RNA-seq experiments with HISAT, StringTie and Ballgown. *Nat. Protoc.* **11**, 1650–1667. <https://doi.org/10.1038/nprot.2016.095> (2016).
26. Robinson, M. D., McCarthy, D. J. & Smyth, G. K. edgeR: A Bioconductor package for differential expression analysis of digital gene expression data. *Bioinformatics* **26**, 139–140. <https://doi.org/10.1093/bioinformatics/btp616> (2010).
27. Subramanian, A. *et al.* Gene set enrichment analysis: A knowledge-based approach for interpreting genome-wide expression profiles. *Proc. Natl. Acad. Sci. USA* **102**, 15545–15550. <https://doi.org/10.1073/pnas.0506580102> (2005).
28. Newman, A. M. *et al.* Determining cell type abundance and expression from bulk tissues with digital cytometry. *Nat. Biotechnol.* **37**, 773–782. <https://doi.org/10.1038/s41587-019-0114-2> (2019).
29. Newman, A. M. *et al.* Robust enumeration of cell subsets from tissue expression profiles. *Nat. Methods* **12**, 453–457. <https://doi.org/10.1038/nmeth.3337> (2015).
30. Kobayashi, M. *et al.* Ovarian cancer cell invasiveness is associated with discordant exosomal sequestration of Let-7 miRNA and miR-200. *J. Transl. Med.* **12**, 4. <https://doi.org/10.1186/1479-5876-12-4> (2014).
31. Taube, J. M. *et al.* Association of PD-1, PD-1 ligands, and other features of the tumor immune microenvironment with response to anti-PD-1 therapy. *Clin. Cancer Res.* **20**, 5064–5074. <https://doi.org/10.1158/1078-0432.CCR-13-3271> (2014).
32. Nagatani, M. *et al.* Comparison of biological features between severely immuno-deficient NOD/Shi-scid Il2rg(null) and NOD/LtSz-scid Il2rg(null) mice. *Exp. Anim.* **68**, 471–482. <https://doi.org/10.1538/expanim.19-0024> (2019).
33. Pawlowska, A. *et al.* Current understanding on why ovarian cancer is resistant to immune checkpoint inhibitors. *Int. J. Mol. Sci.* <https://doi.org/10.3390/ijms241310859> (2023).
34. Lo Russo, G. *et al.* Antibody-Fc/FcR interaction on macrophages as a mechanism for hyperprogressive disease in non-small cell lung cancer subsequent to PD-1/PD-L1 blockade. *Clin. Cancer Res.* **25**, 989–999. <https://doi.org/10.1158/1078-0432.CCR-18-1390> (2019).
35. Wang, M. *et al.* Humanized mice in studying efficacy and mechanisms of PD-1-targeted cancer immunotherapy. *FASEB J.* **32**, 1537–1549. <https://doi.org/10.1096/fj.201700740R> (2018).
36. Capasso, A. *et al.* Characterization of immune responses to anti-PD-1 mono and combination immunotherapy in hematopoietic humanized mice implanted with tumor xenografts. *J. Immunother. Cancer* **7**, 37. <https://doi.org/10.1186/s40425-019-0518-z> (2019).
37. Zhou, J. *et al.* Clinical significance of CD38 and CD101 expression in PD-1(+)CD8(+) T cells in patients with epithelial ovarian cancer. *Oncol. Lett.* **20**, 724–732. <https://doi.org/10.3892/ol.2020.11580> (2020).
38. Quan, Q., Xiong, X., Wu, S. & Yu, M. Identification of immune-related key genes in ovarian cancer based on WGCNA. *Front. Genet.* **12**, 760225. <https://doi.org/10.3389/fgene.2021.760225> (2021).
39. Moran, B., Davern, M., Reynolds, J. V., Donlon, N. E. & Lysaght, J. The impact of histone deacetylase inhibitors on immune cells and implications for cancer therapy. *Cancer Lett.* **559**, 216121. <https://doi.org/10.1016/j.canlet.2023.216121> (2023).
40. Mian, S. A., Arjos-Afonso, F. & Bonnet, D. Advances in human immune system mouse models for studying human hematopoiesis and cancer immunotherapy. *Front. Immunol.* **11**, 619236. <https://doi.org/10.3389/fimmu.2020.619236> (2020).
41. Yin, L., Wang, X. J., Chen, D. X., Liu, X. N. & Wang, X. J. Humanized mouse model: A review on preclinical applications for cancer immunotherapy. *Am. J. Cancer Res.* **10**, 4568–4584 (2020).
42. Park, N. *et al.* Preclinical platform for long-term evaluation of immuno-oncology drugs using hCD34+ humanized mouse model. *J. Immunother. Cancer* <https://doi.org/10.1136/jitc-2020-001513> (2020).
43. Katano, I. *et al.* Development of a novel humanized mouse model for improved evaluation of in vivo anti-cancer effects of anti-PD-1 antibody. *Sci. Rep.* **11**, 21087. <https://doi.org/10.1038/s41598-021-00641-8> (2021).
44. Zhang, Y. *et al.* Real-time GFP intravital imaging of the differences in cellular and angiogenic behavior of subcutaneous and orthotopic nude-mouse models of human PC-3 prostate cancer. *J. Cell Biochem.* **117**, 2546–2551. <https://doi.org/10.1002/jcb.25547> (2016).
45. Sallinen, H. *et al.* A highly reproducible xenograft model for human ovarian carcinoma and application of MRI and ultrasound in longitudinal follow-up. *Gynecol. Oncol.* **103**, 315–320. <https://doi.org/10.1016/j.ygyno.2006.03.030> (2006).

46. Hye Jeong, J. *et al.* Orthotopic model of pancreatic cancer using CD34(+) humanized mice and generation of tumor organoids from humanized tumors. *Int. Immunopharmacol.* **121**, 110451. <https://doi.org/10.1016/j.intimp.2023.110451> (2023).
47. Ko, Y., Jeong, Y. H., Seo, J. H. & Lee, J. A. Development of a bioluminescent human osteosarcoma model in humanized NSG mice: A pilot study. *In Vivo* **35**, 2151–2157. <https://doi.org/10.21873/invivo.12485> (2021).
48. Shaw, T. J., Senterman, M. K., Dawson, K., Crane, C. A. & Vanderhyden, B. C. Characterization of intraperitoneal, orthotopic, and metastatic xenograft models of human ovarian cancer. *Mol. Ther.* **10**, 1032–1042. <https://doi.org/10.1016/j.ymthe.2004.08.013> (2004).
49. Takaishi, K. *et al.* Involvement of M2-polarized macrophages in the ascites from advanced epithelial ovarian carcinoma in tumor progression via Stat3 activation. *Cancer Sci.* **101**, 2128–2136. <https://doi.org/10.1111/j.1349-7006.2010.01652.x> (2010).
50. Yuan, X. *et al.* Prognostic significance of tumor-associated macrophages in ovarian cancer: A meta-analysis. *Gynecol. Oncol.* **147**, 181–187. <https://doi.org/10.1016/j.ygyno.2017.07.007> (2017).
51. Zhang, S. *et al.* Analysis of CD8+ Treg cells in patients with ovarian cancer: A possible mechanism for immune impairment. *Cell Mol. Immunol.* **12**, 580–591. <https://doi.org/10.1038/cmi.2015.57> (2015).
52. Tie, Y., Tang, F., Wei, Y. Q. & Wei, X. W. Immunosuppressive cells in cancer: Mechanisms and potential therapeutic targets. *J. Hematol. Oncol.* **15**, 61. <https://doi.org/10.1186/s13045-022-01282-8> (2022).
53. Helmink, B. A. *et al.* B cells and tertiary lymphoid structures promote immunotherapy response. *Nature* **577**, 549–555. <https://doi.org/10.1038/s41586-019-1922-8> (2020).
54. Khabele, D. *et al.* Drug-induced inactivation or gene silencing of class I histone deacetylases suppresses ovarian cancer cell growth: Implications for therapy. *Cancer Biol. Ther.* **6**, 795–801. <https://doi.org/10.4161/cbt.6.5.4007> (2007).
55. Briere, D. *et al.* The class I/IV HDAC inhibitor mocetinostat increases tumor antigen presentation, decreases immune suppressive cell types and augments checkpoint inhibitor therapy. *Cancer Immunol. Immunother.* **67**, 381–392. <https://doi.org/10.1007/s00262-017-2091-y> (2018).
56. Li, X. *et al.* HDAC inhibition potentiates anti-tumor activity of macrophages and enhances anti-PD-L1-mediated tumor suppression. *Oncogene* **40**, 1836–1850. <https://doi.org/10.1038/s41388-020-01636-x> (2021).
57. Szabo, P. M. *et al.* Cancer-associated fibroblasts are the main contributors to epithelial-to-mesenchymal signatures in the tumor microenvironment. *Sci. Rep.* **13**, 3051. <https://doi.org/10.1038/s41598-023-28480-9> (2023).
58. Hussain, A. *et al.* Distinct fibroblast functional states drive clinical outcomes in ovarian cancer and are regulated by TCF21. *J. Exp. Med.* <https://doi.org/10.1084/jem.20191094> (2020).
59. Murakami, R. *et al.* Establishment of a novel histopathological classification of high-grade serous ovarian carcinoma correlated with prognostically distinct gene expression subtypes. *Am. J. Pathol.* **186**, 1103–1113. <https://doi.org/10.1016/j.ajpath.2015.12.029> (2016).
60. Ito, M. *et al.* NOD/SCID/gamma(c)(null) mouse: An excellent recipient mouse model for engraftment of human cells. *Blood* **100**, 3175–3182. <https://doi.org/10.1182/blood-2001-12-0207> (2002).
61. Guo, J. *et al.* Establishment of two ovarian cancer orthotopic xenograft mouse models for in vivo imaging: A comparative study. *Int. J. Oncol.* **51**, 1199–1208. <https://doi.org/10.3892/ijo.2017.4115> (2017).

Acknowledgements

We thank the core facilities of flow cytometry and optical imaging and disease animal resource center at the ConveRgence mEDicine research cenTer (CREDIT), Asan Medical Center for the use of their shared equipment, services and expertise.

Author contributions

S.W.K., J.-Y.L., O.-J.K., and S.-W.L. designed and performed the experiments, and generated the data for the study. S.W.K., Y.-M.K., and S.-W.L. conceived and designed the study. S.W.K. wrote the paper. S.-W.L. performed supervisory roles in conception, direction, and completion of the study. E.K.C. acquired the funding.

Funding

This research was supported by a grant from the Korea Health Technology R&D Project through the Korea Health Industry Development Institute (KHIDI), funded by the Ministry of Health & Welfare, Republic of Korea (grant number: HI20C1586).

Competing interests

The authors declare no competing interests.

Additional information

Supplementary Information The online version contains supplementary material available at <https://doi.org/10.1038/s41598-024-60501-z>.

Correspondence and requests for materials should be addressed to S.-W.L.

Reprints and permissions information is available at www.nature.com/reprints.

Publisher's note Springer Nature remains neutral with regard to jurisdictional claims in published maps and institutional affiliations.



Open Access This article is licensed under a Creative Commons Attribution 4.0 International License, which permits use, sharing, adaptation, distribution and reproduction in any medium or format, as long as you give appropriate credit to the original author(s) and the source, provide a link to the Creative Commons licence, and indicate if changes were made. The images or other third party material in this article are included in the article's Creative Commons licence, unless indicated otherwise in a credit line to the material. If material is not included in the article's Creative Commons licence and your intended use is not permitted by statutory regulation or exceeds the permitted use, you will need to obtain permission directly from the copyright holder. To view a copy of this licence, visit <http://creativecommons.org/licenses/by/4.0/>.

© The Author(s) 2024